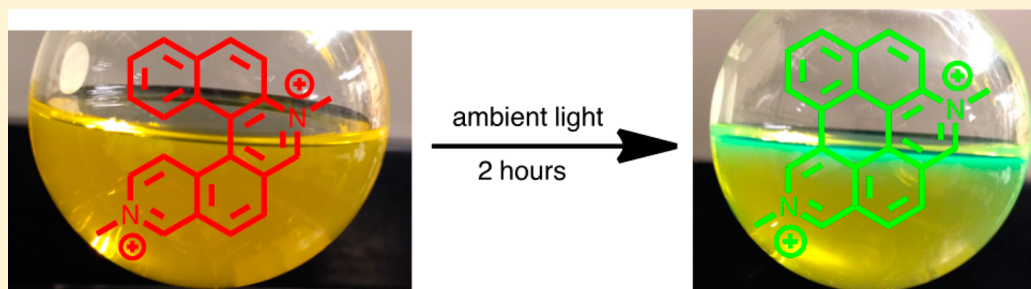


Synthesis, Structure, and Photochemical Behavior of [5]Heli-viologen Isomers

Xiaoping Zhang, Edward L. Clennan,* Navamoney Arulsamy, Rachael Weber, and Jacob Weber

Department of Chemistry, University of Wyoming, Laramie, Wyoming 82071, United States

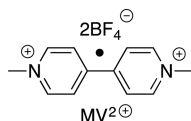
S Supporting Information



ABSTRACT: The syntheses of isomeric helical viologens that have potential applications in supramolecular chemistry and catalysis have been developed. The structures of the molecules and their solid-state packing motifs have been determined by X-ray crystallography. Computational studies demonstrate that the magnitude of their racemization barriers is primarily determined by the identity of the helical scaffold and is insensitive to the placement of the viologen functional group. The isomers are similar in their photophysical behavior but very different in their photochemical behavior.

INTRODUCTION

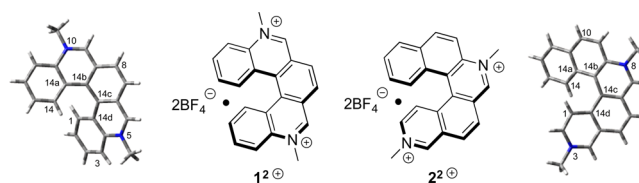
Viologens are the dicationic salts of 4,4'-bipyridine (e.g., MV²⁺).¹ Their applications have dramatically expanded from their early use as herbicides^{2–4} to their use as electron transfer relays,^{5–7} as DNA photocleaving agents,⁸ as components of charge-transfer complexes,^{9–13} in supramolecular assemblies,¹⁴ in polymers,¹⁵ and as integral components of molecular electronic devices,¹⁶ such as sensors^{17–19} and electrochromic switches.²⁰



The interest in viologens is likely to remain high given the recent recognition that fluorescent organic salts have many favorable characteristics^{21,22} for device construction and the reports that viologens may function as potent and novel photoacids.^{23–25} Unfortunately, despite the fact that photo-reduction of MV²⁺ has been known for many years, photophysical and photochemical studies of viologens are rare. In addition, Lin and Zhou²⁶ have recently pointed out that there is a paucity of viologens with extended π -conjugation, a design element that can be used to fine-tune their photochemical and electrochemical properties.

In order to address this gap in the structural landscape of viologens, we report here the synthesis, structural characterization, photophysics, and photochemistry of a novel isomeric pair of π -extended helical viologens, 5,10-dimethyl-5,10-

diaza[5]helicene bis-tetrafluoroborate²⁷ and 3,8-dimethyl-3,8-diaza[5]helicene bis-tetrafluoroborate (**1**²⁺ and **2**²⁺).²⁷ These represent rare examples of chiral viologens^{15,28–31} and the first examples that we are aware of in which the chirality is due to the polyaromatic backbone. These compounds also complete the link, first established by the fascinating helquats,^{32–35} between helicenes and viologens.

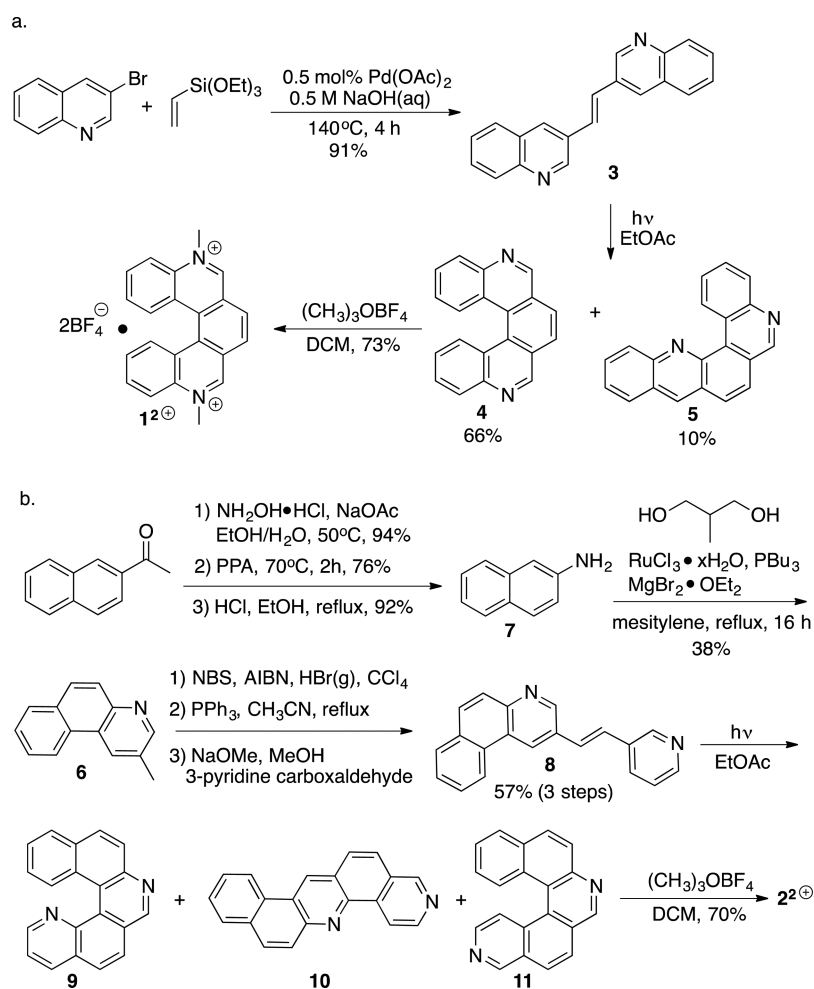


RESULTS AND DISCUSSION

Synthesis. Heli[5]viologen **1**²⁺ was readily available by alkylation of the known 5,10-diaza[5]helicene³⁶ that was prepared by the slightly modified route shown in Scheme 1a. 1,2-Bis(3-quinoyl)ethene (**3**) was generated by a Hiyama–Heck Pd-catalyzed cross-coupling reaction between triethoxyvinylsilane and 2 equiv of 3-bromoquinoline.^{37,38} Photolysis of **3** with a Pyrex-filtered medium-pressure Hanovia lamp generated a mixture of 5,10-diaza[5]helicene (**4**) and benzo[*b*]-1,8-diaza[4]helicene (**5**), which was separated and purified by column chromatography. Alkylation of the major product **4**

Received: April 13, 2016

Published: June 10, 2016

Scheme 1. Synthesis of 1^{2+} and 2^{2+} Table 1. Comparison of X-ray and B3LYP/6-311+G(2d,p) Structural Parameters^a

	12^b	4	1^{2+}	11	2^{2+}
$\Theta_{14,14a,14b,14c}$ deg	18.2 (17.5)	17.0	17.1 (17.2)	19.2	21.7 (16.0)
$\Theta_{14a,14b,14c,14d}$ deg	30.2 (30.3)	27.9	29.8 (33.8)	28.0	27.9 (26.8)
$\Theta_{1,14d,14c,14b}$ deg	18.1 (17.3)	17.0	17.0 (17.2)	15.9	17.2 (21.9)
d_{py-py}^c Å	–	1.45	1.45 (1.44)	1.45	1.46 (1.45)
$d_{1H,14H}^d$ Å	2.63 (2.54)	2.49	2.57 (2.65)	2.53	2.66 (2.49)
$d_{1,14}$ Å	2.96 (2.90)	3.00	3.01 (3.03)	2.99	2.99 (2.91)
$d_{4a,5}$ ($d_{4a,N}$), ^d Å	1.43 (1.42)	1.38	1.40 (1.40)	–	–
$d_{5,6}$ ($d_{N,6}$), ^d Å	1.36 (1.35)	1.30	1.32 (1.31)	–	–
$d_{2,3}$ ($d_{2,N}$), ^e Å	1.40 (1.40)	–	–	1.35	1.37 (1.37)
$d_{3,4}$ ($d_{N,4}$), ^e Å	1.37 (1.36)	–	–	1.31	1.33 (1.32)
$d_{7,8}$ ($d_{7,N}$), ^e Å	1.36 (1.35)	–	–	1.30	1.32 (1.32)
$d_{8,8a}$ ($d_{N,8a}$), ^e Å	1.42 (1.42)	–	–	1.37	1.39 (1.39)

^aX-ray data in parentheses. ^b[5]Helicene. ^cLength of bond connecting two pyridinium rings. ^dCarbon–nitrogen bond lengths in 1^{2+} . ^eCarbon–nitrogen bond lengths in 2^{2+} .

with Meerweins' salt³⁹ (trimethyloxonium tetrafluoroborate) generated the heli-viologen 1^{2+} in a modest but acceptable 73% yield. Attempts to alkylate 4 with methyl iodide or with dimethyl sulfate [(MeO)₂SO₂] failed. In each case, the monomethylated helicene was obtained even in the presence of excess alkylating agent. The same monomethylated helicene, albeit with a different counterion (BF₄[−]), was obtained by refluxing a solution of 1^{2+} in aqueous sodium hydroxide.

The synthetic route used to make 3,8-dimethyl-3,8-diaza[5]-helicene (2^{2+}) is depicted in Scheme 1b. The key intermediate in this reaction sequence is (3-methyl)benzo[*f*]quinoline (6), which was made in a ruthenium-catalyzed cyclocondensation reaction between 2-naphthylamine (7) and 2-methyl-1,3-propanediol.⁴⁰ Conversion of 6 to (*E*)-1-(benzo[*f*]quinolin-3-yl)-2-(3-pyridyl)ethene (8) was accomplished by the three-step Wittig reaction protocol shown in Scheme 1b. Including gaseous HBr in the free-radical bromination step (NBS/AIBN)

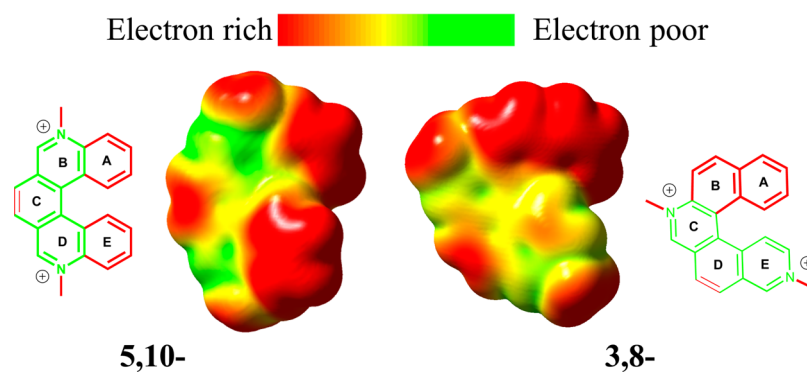


Figure 1. Electrostatic potential energy surfaces (B3LYP/6-311+G(2d,p)) for heli-viologens 1^{2+} and 2^{2+} .

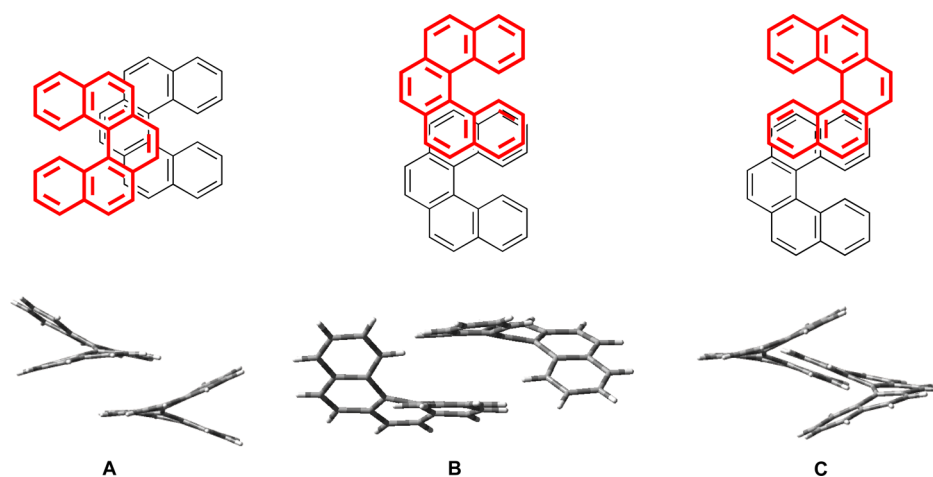


Figure 2. Stacking motifs A, B, and C adopted by aza- and diaza[5]helicenes.

was required in order to protonate the nitrogen and suppress oligomerization. The (3-bromomethyl)benzo[*f*]quinoline hydrobromide product was then dried and used directly in the next step to make the phosphonium salt that was subsequently used in the Wittig reaction with 3-pyridine carboxaldehyde. The Mallory photocyclization⁴¹ of **8** generated 1,8-diaza[5]helicene (**9**), naphtha[2,1-*b*][1,8]phenanthroline (**10**), and 3,8-diaza[5]helicene (**11**), in 35%, 18%, and 38% yields, respectively, after chromatographic separation. Helicene **11** was then converted into 2^{2+} in 70% yield by alkylation with trimethyloxonium tetrafluoroborate.

Structural Characterization. The structures of 1^{2+} and 2^{2+} are completely consistent with their spectral data (see [Experimental Section](#)) and were confirmed by X-ray crystallography. The key crystal structure features of 1^{2+} and 2^{2+} are compared to those of [5]helicene and to B3LYP/6-311+G-(2d,p)-computed values for [5]helicene and for the bipyridine precursors **4** and **11** of viologens 1^{2+} and 2^{2+} , respectively, in [Table 1](#).

The structural features of the helicenes listed in [Table 1](#) are very similar in many respects. The only substantial differences are in the fjord regions, the boundaries of which are defined by the dihedral angles $\Theta_{14,14a,14b,14c}$, $\Theta_{14a,14b,14c,14d}$, and $\Theta_{1,14d,14c,14b}$. The middle dihedral angle, $\Theta_{14a,14b,14c,14d}$ in the fjord regions of all the helicenes is substantially larger than the outer adjacent dihedral angles, $\Theta_{14,14a,14b,14c}$ and $\Theta_{1,14d,14c,14b}$, consistent with the middle aromatic ring of the helicene suffering the greatest deformation from the preferred planar geometry. The largest change in the fjord regions that occurs upon alkylation of the

bipyridine precursors, $4 \rightarrow 1^{2+}$ and $11 \rightarrow 2^{2+}$, is associated with the viologen torsional angle, $\Theta_{14a,14b,14c,14d}$ and $\Theta_{1,14d,14c,14b}$, respectively. In the case of $4 \rightarrow 1^{2+}$, the viologen torsional angle increases by 1.9° ($27.9^\circ \rightarrow 29.8^\circ$), while the other two fjord region dihedral angles stay the same or only increase by 0.2° ($17.0^\circ \rightarrow 17.2^\circ$). In the case of $11 \rightarrow 2^{2+}$, the viologen torsional angle increases by 1.3° ($15.9^\circ \rightarrow 17.2^\circ$), while the other two fjord dihedral angles decrease by 0.1° and increase by 2.5° . These changes in the viologen torsional angle reflect the electronic driving force to minimize the overlap between the two positively charged *N*-methylpyridinium groups. In the case of the unconstrained methyl viologen, MV^{2+} , with weakly interacting counterions, such as BF_4^- , the optimal dihedral angle that provides a balance between energetically favorable resonance overlap and energetically destabilizing positive charge interaction appears to be near 40° .¹⁴

The X-ray data reveal that the C_1-C_{14} ($d_{1,14}$) and H_1-H_{14} ($d_{H1,H14}$) distances are both substantially shorter in the 3,8-viologen than in the 5,10-isomer. The location of the viologen functional group within the [5]helicene scaffold coupled with its preferred torsional angle (vide supra) undoubtedly contributes to this difference. However, we cannot unequivocally rule out a small contribution from a more favorable electrostatic interaction between the terminal A and E rings in the 3,8-viologen than in the 5,10-viologen ([Figure 1](#)).

Macchi and co-workers⁴² recently reported a study of the crystalline packing of a large number of aza- and diaza[5]helicenes, including that of 5,10-diaza[5]helicene (**4**). They

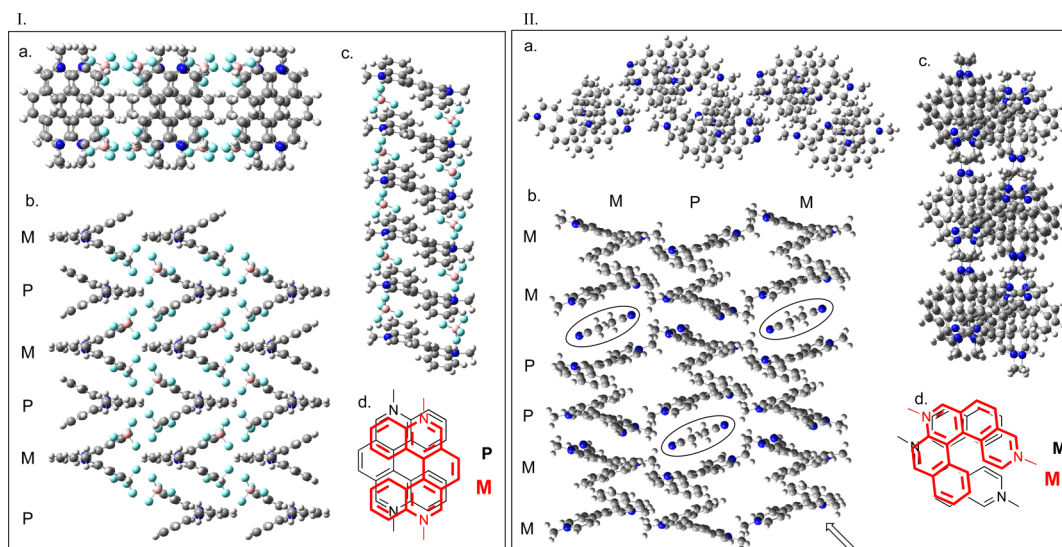


Figure 3. Crystal packing projections for 1^{2+} (I) and 2^{2+} (II) and their stacking motifs Id and IId.

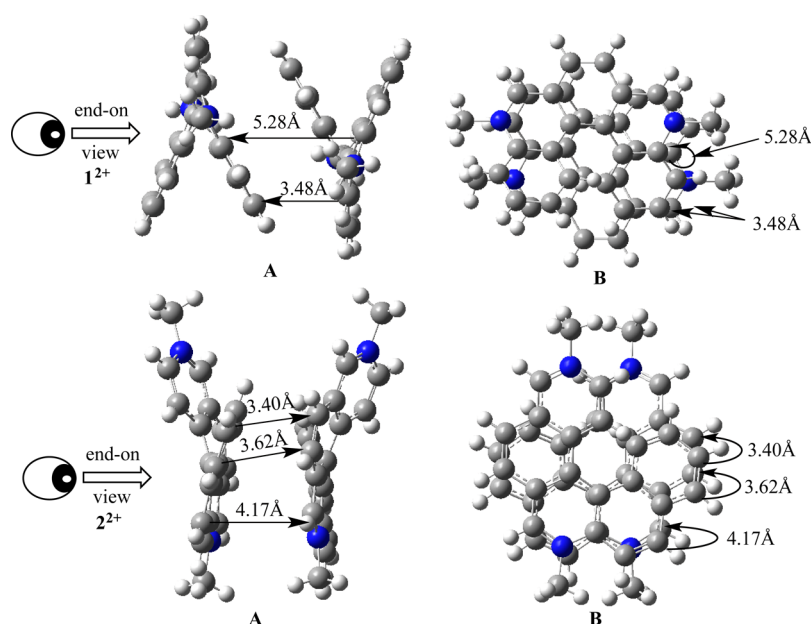


Figure 4. Side-on (A) and end-on (B) views showing close contacts between crystal-packing molecular pairs $1^{2+}/1^{2+}$ and $2^{2+}/2^{2+}$.

reported that these azahelicenes frequently adopted one of three stacking motifs, as shown in Figure 2.

Heli-viologens 1^{2+} and 2^{2+} , however, do not adopt any of these established packing motifs but instead the unusual packing arrangements shown in Figure 3. Heli-viologen 1^{2+} has C_2 molecular symmetry and forms a crystal that belongs to the centrosymmetric orthorhombic space group $Pbcn$ (Figure 3, I). Heli-viologen 2^{2+} lacks the C_2 molecular symmetry and forms a crystal that belongs to the centrosymmetric monoclinic space group $C2/c$. Both crystals are achiral. Three projections of the crystal packing of an array of 16 molecules of 1^{2+} (a, b, and c) are depicted in the left-hand box in Figure 3. The heli-viologens are arranged in three straight columns that alternate in stereochemistry from top to bottom, as shown to the left of projection Ib. The horizontal rows consist of a single enantiomer, M or P, with the fjord regions pointing in the opposite direction in adjacent rows. Two BF_4^- are located on opposite faces of 1^{2+} at a B–N distance of 3.45 Å. The BF_4^- are

not centered directly over the pyridinium ring but are displaced toward the periphery of the viologen so that the nearest interaction is with the CH ring carbon α to nitrogen at a distance of 3.41 Å. This simultaneously places the BF_4^- 4.85 Å above the external rim of the terminal ring of an adjacent helicene in the –M–P–M–P– columnar array of heli-viologens (Figure 3, Ib). In addition, all the BF_4^- are located adjacent to the interstitial space between the columns and experience two additional “in-plane” cross-column B–CH interactions of 3.85 and 4.30 Å.

Three projections of the crystal packing of an array of 18 molecules of 2^{2+} are depicted in the right-hand box in Figure 3. The BF_4^- counterions are disordered and have been removed from the packing array for clarity. A striking feature of the crystal, which distinguishes it from 1^{2+} , is the pairwise packing of the 2^{2+} molecules. Both molecules in the pair have the same stereochemistry and alternate, (M/M)–(P/P)–(M/M), along the length of the column. Two molecules of acetonitrile, the

solvent used to grow the crystal of 2^{2+} , are intercalated into the void in the crystal structure between each $2^{2+}/2^{2+}$ pair. Three of these acetonitrile partners are identified in projection IIb by enclosing them in ovals. The columns, unlike that observed for 1^{2+} , are not straight but adopt a herringbone-like structure, as depicted in projection IIa, which is a view down the diagonal of the 18 molecule array, as shown by the arrow on projection IIb.

The stacking motifs for 1^{2+} and 2^{2+} (d in both boxes in Figure 3) are characterized by enhanced molecular surface area contact via π - π stacking in comparison to the aza-helicenes (A, B, and C in Figure 2). Perfect sandwich-like packing is not observed for the heli-viologens (see Figure 4) because of the nonplanar topography of the helicenes, however, several π -surface contacts of less than 4 Å are observed (Figure 4). The near parallel arrangements of the bipyridinium ion functional groups in the packing motifs (Figure 3, Id and IId) suggest that the alignment of molecular dipoles and electrostatic interactions plays a role in the crystal packing. In each case, the electron-rich portion of the heli-viologen, as determined by the electrostatic potential energy surfaces shown in Figure 1, overlaps with the electron-poor surface of its partner. These attractive interactions compensate for the repulsive closed-shell π -cloud interactions and are the driving force for adoption of these unusual packing arrangements.⁴³

Dynamic Behavior. Heli-viologens 1^{2+} and 2^{2+} , like their carbocyclic analogues, are chiral as a result of their helical structures. However, in analogy to other hetero[5]helicenes, rapid room-temperature conformational deformations are likely to limit the enantiomer lifetimes to a few minutes at room temperature, making studies of resolved samples difficult.⁴⁴ Consequently, we have initially chosen to limit our studies of this important process with 1^{2+} and 2^{2+} to a series of computational investigations. Previous computational studies of [5]helicene racemizations have focused on planar (C_{2v}) and saddle-like (C_s) transition states that can relax with equal probability to the P and M enantiomers. We will not consider potential reversible bond-making–bond-breaking racemization mechanisms, despite the fact that they have been considered⁴⁵ and experimental evidence for a chemical pathway for racemization has even been reported.⁴⁶ These chemical pathways are exceedingly rare and unlikely to occur with these heli-viologens.

The transition states for racemizations of 1^{2+} and 2^{2+} were located with the B3LYP/6-311+G(2d,p) computational method and adopt saddle-like structures, as depicted in Figure 5. The B3LYP/6-311+G(2d,p) barriers for racemization of 1^{2+} and 2^{2+} along with those for several other [5]helicene homologues are collected and compared in Table 2.

The activation barriers (Table 2) were calculated from the differences in energies of the optimized helicene and corresponding transition state and are corrected for zero-point energies and thermal effects. The transition states were located using the synchronous transition-guided quasi-Newton

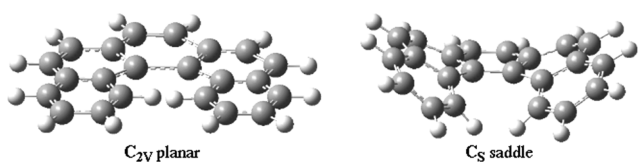


Figure 5. Planar (C_{2v}) and saddle-like (C_s) transition states (B3LYP/6-311+G(2d,p) for racemizations.

Table 2. B3LYP/6-311+G(2d,p) Racemization Barriers for Helicenes

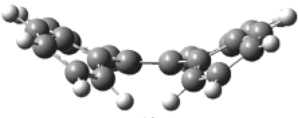
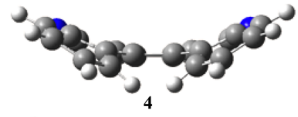
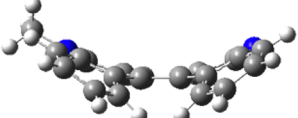
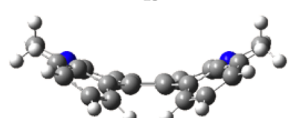
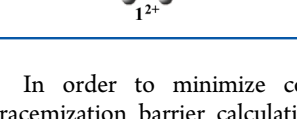
compd	$\Delta G_{\text{calc}}^{\ddagger}$ (kcal mol ⁻¹)	compd	$\Delta G_{\text{calc}}^{\ddagger}$ (kcal mol ⁻¹)
12 ^b	23.1	14 ^d	20.5
4	19.6	11 ^e	19.6
13 ^{+c}	20.0	2 ²⁺ e	20.2
1 ²⁺	21.2	1 ²⁺ ·BF ₄ ^{-ef}	20.3

^aGibbs free energies at 25 °C calculated from potential energies and adjusted for zero-point energies and thermal corrections. ^b[5]-Helicene. ^cN-Methyl-5,10-diaza[5]helicene. ^d5,10-Diaza[5]helicene bis-N-oxide. ^eChiral transition state entropic correction of $R \ln 2$. ^fanti-Bis-tetrafluoroborate salt (see the text).

(STQN) method in conjunction with the B3LYP/6-311+G(2d,p) computation method. The activation barriers for the 3,8-diaza[5]helicenes 11, 2^{2+} , and 2^{2+} ·BF₄⁻ were adjusted by an entropic contribution of $R \ln 2$ to correct for reaction through enantiomeric transition states.

The gas-phase racemization barrier for [5]helicene (12) (Table 2) is 1 kcal/mol lower than the experimental value measured in naphthalene at 188 °C.⁴⁷ Replacement of two benzene rings with pyridines to give 5,10-diaza[5]helicene (4) decreased the racemization barrier by 3.5 kcal/mol. Vacek Chocholoušová and co-workers⁴⁴ reported a B3LYP/cc-pVTZ racemization barrier of 22.2 kcal/mol for 2-aza[5]helicene, a decrease of 1.4 kcal/mol from their calculated value for 12, which involved replacement of one terminal benzene with a pyridine ring. The benzene rings in 12 and the nitrogen-containing rings in both 4 and 2-aza[5]helicene are deformed in their saddle-like racemization transition states from their idealized planar geometries. Consequently, the decrease in the racemization barriers in the aza-helicenes in comparison to the carbocyclic [5]helicene could reflect the 8 kcal/mol smaller pyridine resonance energy than that of benzene.⁴⁸ The racemization barrier for the monomethylated N-methyl-5,10-diaza[5]helicene (13⁺), is 1.2 kcal/mol smaller than that for the corresponding viologen (1²⁺) but only 0.4 kcal/mol larger than the barrier for its bipyridine precursor (4). On the other hand, Vacek Chocholoušová and co-workers⁴⁴ reported that the racemization barrier for monoprotonated 2,13-diaza[5]helicene is 5.7 kcal/mol smaller than that for its free base. The origin of the difference between Vacek Chocholoušová et al.'s results and ours is not entirely clear; however, we note that they report that the transition state for racemization of protonated 2,13-diaza[5]helicene is far from the common saddle-shaped (C_s) structure and could be best characterized as a distorted helix. In contrast, as shown in Table 3, when the nitrogens are not in the terminal ring of the [5]helicene, both the B3LYP/6-311+G(2d,p) mono- and dimethylated transition states adopt the idealized saddle-like topology. The four structural features in the transition states that deviate most from those observed in the P and M helices are the H-1/H-14 distance ($d_{\text{H1,H14}}$) and the three internal dihedral angles in the fjord region ($\Theta_{14a,14b,14c,14d}$, $\Theta_{1,14d,14c,14b}$, and $\Theta_{14,14a,14b,14c}$) (Table 3). Racemization leads to a significant decrease in the H-1 and H-14 distances to the point where they become approximately 1 Å closer in the saddle-like transition states than in the helical energy minima. Simultaneously, the central ring flattens considerably and the arms of the helicene twist to form the sides of the saddle, as revealed by the changes in the dihedral angles in the fjord region (Table 3).

Table 3. Racemization Transition States (TS) and Helical Precursors (P/M) Key Structural Feature Differences

	$d_{1H,14H}$	TS	P/M
	$>_{14a, 14b, 14c, 14d}$	1.55 Å	2.63 Å
	$>_{1, 14d, 14c, 14b}$	0.10°	30.22°
	$>_{14, 14a, 14b, 14c}$	39.24°	18.06°
	$d_{1H,14H}$	TS	P/M
	$>_{14a, 14b, 14c, 14d}$	1.52 Å	2.49 Å
	$>_{1, 14d, 14c, 14b}$	0.00°	27.89°
	$>_{14, 14a, 14b, 14c}$	33.29°	16.96°
	$d_{1H,14H}$	TS	P/M
	$>_{14a, 14b, 14c, 14d}$	1.55 Å	2.55 Å
	$>_{1, 14d, 14c, 14b}$	2.41°	28.04°
	$>_{14, 14a, 14b, 14c}$	33.64°	17.38°
	$d_{1H,14H}$	TS	P/M
	$>_{14a, 14b, 14c, 14d}$	1.54 Å	2.57 Å
	$>_{1, 14d, 14c, 14b}$	0.01°	29.80°
	$>_{14, 14a, 14b, 14c}$	35.18°	17.01°
	$d_{1H,14H}$	TS	P/M
	$>_{14a, 14b, 14c, 14d}$	1.54 Å	2.57 Å
	$>_{1, 14d, 14c, 14b}$	0.01°	29.80°
	$>_{14, 14a, 14b, 14c}$	35.18°	17.06°

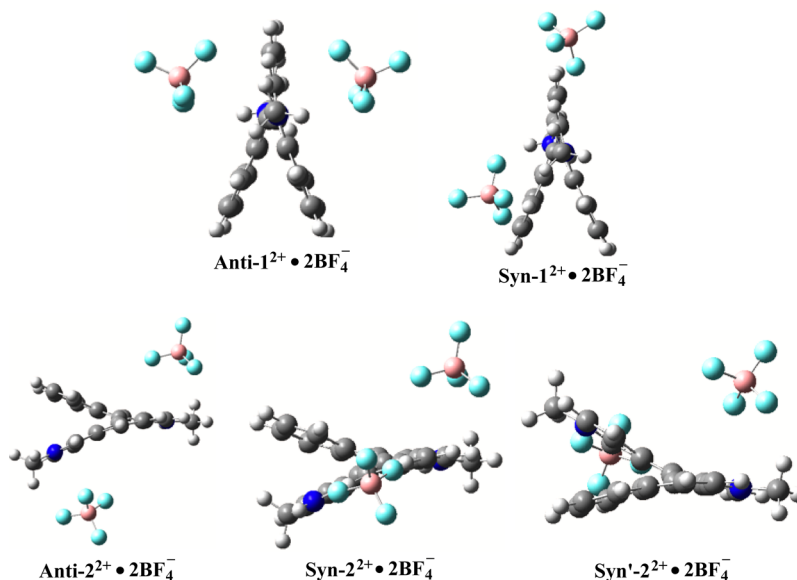
In order to minimize computation expense, our initial racemization barrier calculations with 13^+ , 12^+ , and 2^+ were gas-phase calculations in the absence of solvent and counterion (e.g., BF_4^-). Consequently, these barriers (Table 2) can be considered intrinsic barriers that can be compared to experimental values in order to determine the influence of solvent and counterion on barrier height. We have done some ion pair calculations and indeed found them to be difficult and time-consuming optimizations. As anticipated, several tetrafluoroborate salt optimized structures for 1^+ and 2^+ can be located, but we cannot be certain that we have located the global minimum. The energy minima we have located are shown in Figure 6.

anti- And *syn*-bis-tetrafluoroborate salts were identified as energy minima in acetonitrile on both the 1^+ - $2BF_4^-$ and 2^+ - $2BF_4^-$ potential energy surfaces using B3LYP/6-311+G(2d,p) and the polarizable continuum model. (Figure 6). In the *anti*-

structures, the BF_4^- are located on opposite faces of the helical dication. In *anti*- 1^+ - $2BF_4^-$, the anions are displaced from the center of the pyridinium rings out toward the periphery of the helicene scaffold above the N_5-C_6 and $N_{10}-C_9$ bonds with B–N contact distances of 3.59 Å and C_6-F and C_9-F closest contact distances of 3.07 and 3.02 Å, respectively. The BF_4^- adopt remarkably similar locations relative to the pyridinium rings in *anti*- 2^+ - $2BF_4^-$, with B– N_3 and B– N_8 contact distances of 3.61 and 3.58 Å, respectively, and identical C_4-F and C_7-F close contact distances of 3.05 Å.

In the *syn*-structures, one BF_4^- adopts a location similar to that observed in the *anti*- isomers, while the other BF_4^- is found in the plane of a pyridinium ring in close contact distance with $N-C_{\alpha}H$. In *syn*- 1^+ - $2BF_4^-$, the in-plane anion exhibits a B–N contact distance of 4.76 Å and an even shorter B– C_6 contact distance of 3.95 Å. The *syn*-structural motif offers the possibility of population of diastereomers. These diastereomeric salts were located on the PES for *syn*- 2^+ - $2BF_4^-$, as depicted in Figure 6 as the *syn*- and *syn'*-structures. The *syn'*-isomer is the more stable diastereomer by 0.09 kcal/mol. The *anti*-isomers in both 1^+ - $2BF_4^-$ and 2^+ - $2BF_4^-$ were less stable than the *syn*-isomers [ZPE-corrected stability order: *syn'*- 2^+ - $2BF_4^-$ (0 kcal/mol) > *syn*- 2^+ - $2BF_4^-$ (0.09 kcal/mol) > *syn*- 1^+ - $2BF_4^-$ (0.73 kcal/mol) > *anti*- 2^+ - $2BF_4^-$ (1.28 kcal/mol) > *anti*- 1^+ - $2BF_4^-$ (2.26 kcal/mol)].

The only transition state that we were able to locate for racemization was for the $P(anti-1^+-2BF_4^-) \rightleftharpoons M(anti-1^+-2BF_4^-)$ interconversion (Figure 7). The transition state adopts a saddle-like structure similar to those shown in Table 3. A comparison of the key structural parameters $d_{1H,14H}$ (1.55 Å), $\Theta_{14a,14b,14c,14d}$ (0.20°), $\Theta_{1,14d,14c,14b}$ (36.94°), and $\Theta_{14,14a,14b,14c}$ (37.20°) to those in Table 3 reveals a small BF_4^- -induced narrowing of the saddle, leading to a decrease in the N–N distance from 6.80 to 6.72 Å. The BF_4^- counterions in the transition state adopt nearly identical positions over the pyridinium rings, as observed in the P or M enantiomer. One BF_4^- is on the concave surface of the saddle (“in-the-saddle”) with a B–N contact distance of 3.59 Å, and the second BF_4^- is on the convex surface of the saddle with a B–N contact distance of 3.60 Å. The racemization barrier decreases by 0.5

**Figure 6.** B3LYP/6-311+G(2d,p)-optimized 1^+ and 2^+ bis-tetrafluoroborate salt energy minima in CH_3CN .

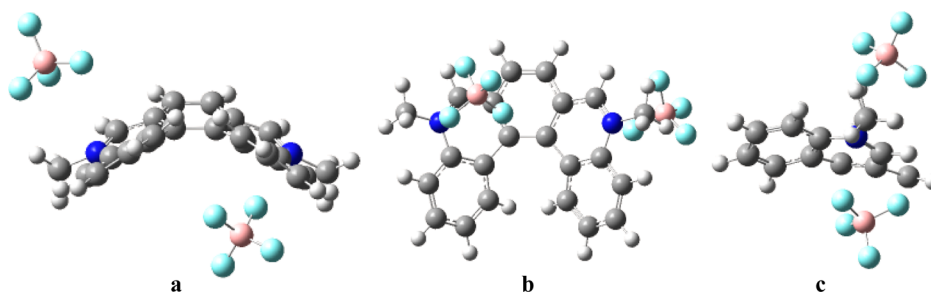
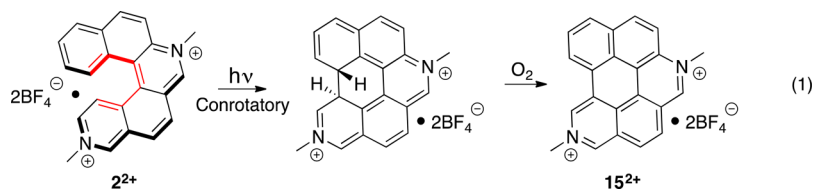


Figure 7. (a) End-on, (b) face-on, and (c) side-on views of the $anti\text{-}1^{2+} \cdot 2BF_4^{-}$ transition state for racemization.



kcal/mol in comparison to the counterion free gas-phase value listed in Table 2.

Photochemistry. The isomeric viologens 1^{2+} and 2^{2+} exhibit remarkably different photochemical behavior. The 5,10-viologen 1^{2+} is photochemically inert when exposed to either ambient light or light from a 600 W halogen lamp. The 3,8-viologen 2^{2+} , on the other hand, reacted under identical conditions within a few hours to generate (2,7-dimethyl-2,7-diaza)benzo[*ghi*]perylene bis-tetrafluoroborate (15^{2+}), in quantitative yield (eq 1). The formation of 15^{2+} during irradiation was easily detected by its bright green fluorescence. Very low solubility precluded collection of the ^{13}C NMR of 15^{2+} . However, the identity of 15^{2+} was established by comparing its calculated [GIAO B3LYP/6-311+G(2d,p)] and experimental ^1H NMR (Figure 8) and by a MALDI-TOF/TOF exact mass determination (see Experimental Section).

major contributor to S_1 (vide infra), can undergo conrotatory closure without generating a phase discontinuity (i.e., only 2^{2+} can maintain maximum overlap during the reaction) (Figure 9).

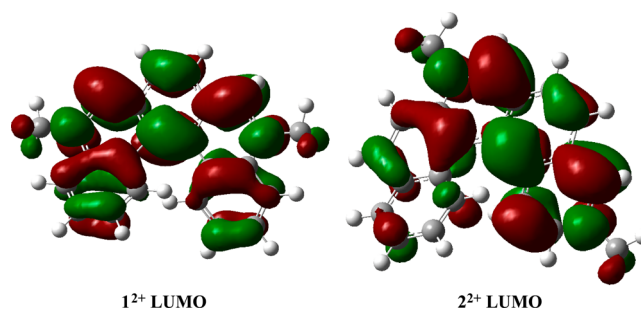


Figure 9. LUMOs of 1^{2+} and 2^{2+} .

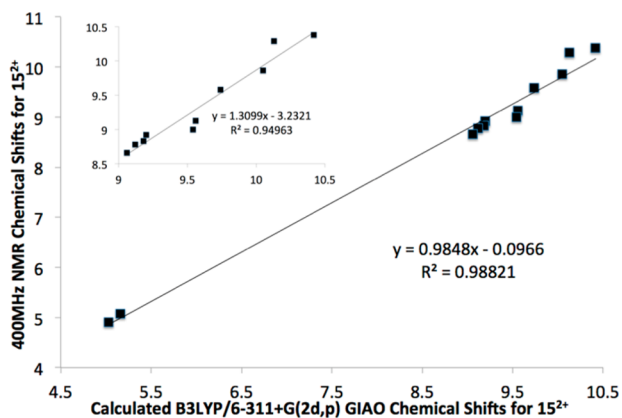


Figure 8. Calculated versus experimental chemical shifts of 15^{2+} . Inset: Expanded downfield region.

The closure of 2^{2+} can be viewed as a symmetry-allowed 6π electron conrotatory electrocyclic reaction of the red 1,3,5-hexatriene unit shown in eq 1. The *trans*-dihydro product of a conrotatory closure is 7.0 kcal/mol more stable than the *cis*-dihydro product, which would form in a disallowed disrotatory closure of 2^{2+} [B3LYP/6-311+G(2d,p)]. A conrotatory closure also provides a rationale for the different photochemical reactivity of 1^{2+} and 2^{2+} ; only the LUMO of 2^{2+} , which is the

Photophysical Characterization. The photophysical data collected for 1^{2+} and 2^{2+} and their bipyridine precursors **4** and **11** are compared in Table 4. The UV–visible spectra of viologens 1^{2+} and 2^{2+} are depicted as solid lines and those of their bipyridine precursors **4** and **11** as dashed lines of the same color in Figure 10. For comparison, the UV–visible spectrum of 5,10-diaza[5]helicene bis-*N*-oxide (**14**) is also displayed in Figure 10 as a green line.

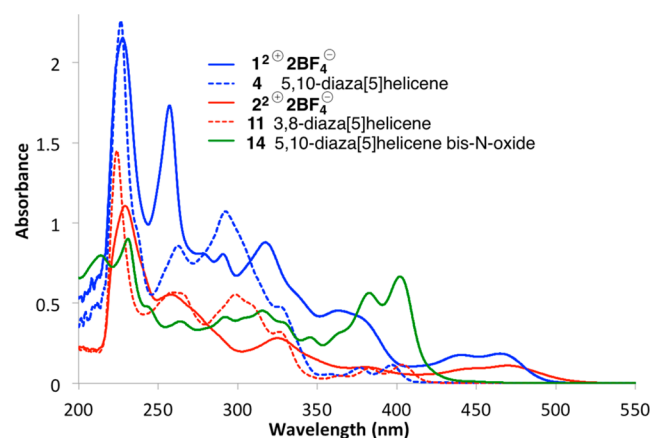
Time domain DFT calculations at the B3LYP/6-311+G(2d,p) computational level were used to assign the most bathochromic envelope of peaks to the $S_0 \rightarrow S_1$ transitions. Despite the different placement of nitrogens in the helical scaffold, the wavelengths and fine structure for these envelope of peaks are remarkably similar for the two viologens 1^{2+} and 2^{2+} (Table 4). In addition, the lowest energy absorption bands for 1^{2+} and 2^{2+} are shifted bathochromically by a nearly identical 68 and 67 nm, respectively, from the lowest energy peak in their bipyridine precursors **4** and **11**. The vibronic progressions are more sharply defined in the bipyridines than in the corresponding viologen. The energy separations are approximately $1200\text{--}1300\text{ cm}^{-1}$, as anticipated for in-plane C–H bends and/or aromatic C–C stretches.⁴⁹

The agreement between the experimental and DFT-calculated positions of the $S_0 \rightarrow S_1$ transitions in both 1^{2+} and 2^{2+} was very sensitive to the computational medium. In the gas phase the lowest energy bands in the TD-DFT calculations

Table 4. Photophysical Data for Heli-Viologens 1^{2+} and 2^{2+} and Their Bipyridine Precursors **4** and **11**^a

	1^{2+}	2^{2+}	4	11
UV-vis ($\epsilon \times 10^{-4}$) ^b	465 (0.40) 441 (0.38)	470 (0.60) 449 (0.49)	397 (0.30) 377 (0.38) 358 (0.15)	403 (0.53) 383 (0.42) 364 (0.21)
λ_F^c	504	566	408, 431, 455	420, 436, 463
λ_{Phos}^c	623	616	501, 531, 586	513, 547, 602
Stokes shift ^d	1664	3609	679	1004
τ_F^e	5.8 ± 0.6	10.2 ± 0.6	6.3 ± 0.6	4.2 ± 0.2
Φ_F	0.066 ± 0.004	0.087 ± 0.001	0.14 ± 0.01	0.18 ± 0.02
τ_{Phos}^f	0.028 ± 0.002	0.088 ± 0.002	1.7	1.2 ± 0.01
k_F^g	11.4×10^6	8.5×10^6	2.2×10^7	4.3×10^7
$E_{S_1}^h$	59.3 ± 0.1	56.5 ± 0.1	71.0 ± 0.1	69.7 ± 0.1
$E_{T_1}^h$	54 ± 2	54 ± 2	57.1 ± 0.2	55.7 ± 0.2
ΔE_{S-T}^h	5.3 ± 2	2.5 ± 2	13.9 ± 0.2	14.0 ± 0.2
band gap ⁱ	2.48(3.03)	2.39(2.59)	2.92(4.01)	2.95(3.84)

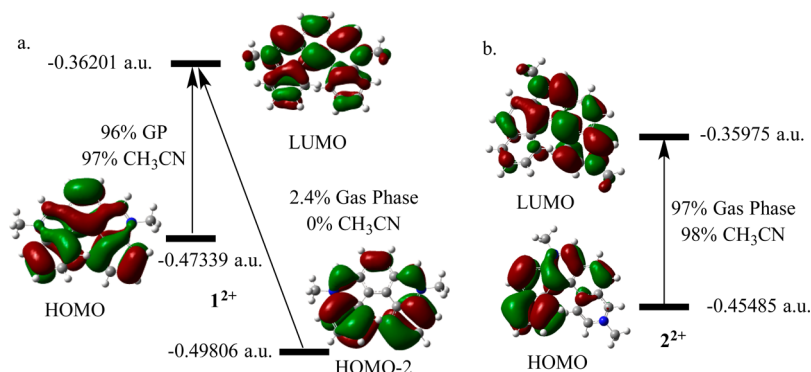
^aIn acetonitrile. ^bExtinction coefficient, in $10^4 \text{ M}^{-1} \text{ cm}^{-1}$. ^cFluorescence wavelength (λ_F) and phosphorescence wavelength (λ_{Phos}), in nanometers. ^dIn wavenumber, cm^{-1} . ^eFluorescence lifetime, in nanoseconds. ^fPhosphorescence lifetime, in seconds. ^gRadiative rate constant, calculated as Φ_F/τ_F . ^hSinglet energy (E_{S_1}), triplet energy (E_{T_1}), and singlet–triplet energy gap (ΔE_{S-T}), in kcal/mol. ⁱOptical gap, in eV. B3LYP/6-311+G(2d,p)-calculated gap in eV is in parentheses.

Figure 10. UV-visible spectra in CH_3CN .

were found at 500 and 597 nm, 35 and 127 nm bathochromic of the experimentally observed wavelengths in 1^{2+} and 2^{2+} , respectively. When the polarizable continuum model was used to include acetonitrile in the calculations, the computed wavelengths (479 and 513 nm) were only 14 and 43 nm bathochromic of the experimental values. In contrast, gas-phase TD-DFT calculations for **4** and **11** predicted absorbances 22

and 13 nm hypsochromic of the experimental values. We attribute the hypersensitivity of the viologens to computational medium to the charge transfer character of the $S_0 \rightarrow S_1$ electronic transitions (Figure 11). The charge transfer character is unmistakable in the HOMO \rightarrow LUMO excitations of 1^{2+} and 2^{2+} (Figure 11). Using these orbitals to assess the extent of charge transfer is valid since the HOMO \rightarrow LUMO determinant is the primary contributor to the excited state density or wave function (Figure 11).⁵⁰ In both cases, the charge transfer is from the relatively electron rich aryl rings to the bipyridinium functional group. This charge transfer is clearly more important in 2^{2+} than in 1^{2+} , providing a rationale for the much larger sensitivity to the computational medium of the $S_0 \rightarrow S_1$ absorption wavelength in 2^{2+} (597 nm \rightarrow 513 nm) than in 1^{2+} (500 nm \rightarrow 479 nm).

The lowest energy envelope of peaks in the absorption spectra of 5,10-diaza[5]helicene bis-*N*-oxide (**14**) (Figure 10) is approximately 70 nm hypsochromic of the $S_0 \rightarrow S_1$ absorption band in 1^{2+} and in appearance is more similar to the absorption spectra of the bipyridine precursors than the viologens. However, the peaks are 6.5 times greater in intensity than the $S_0 \rightarrow S_1$ absorption bands in **4** and **11**. The $S_0 \rightarrow S_1$ band appears at 419 nm with a very low oscillator strength of only 0.0051 with TD-DFT contributions from the HOMO \rightarrow LUMO+1 and the HOMO-1 \rightarrow LUMO determinants of 74%

Figure 11. Dominant determinant contributors to the $S_0 \rightarrow S_1$ band in (a) 1^{2+} and (b) 2^{2+} .

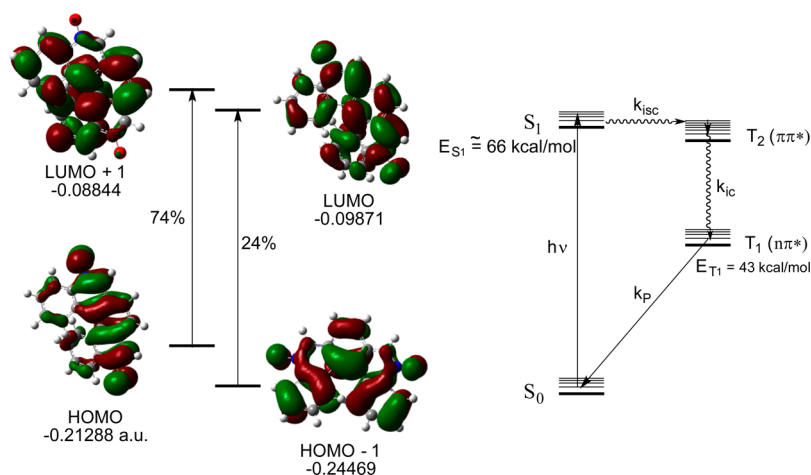


Figure 12. Dominant determinant contributors to $S_0 \rightarrow S_1$ and energy level diagram for **14** showing phantom triplet $T_2(\pi\pi^*)$ and detected triplet $T_1(n\pi^*)$.

and 24%, respectively. In the spectrum of pyridine *N*-oxide, this small band is hidden under a very strong $S_0 \rightarrow S_2$ band.^{51,52} Consistent with a similar interpretation for the absorption spectrum of **14** is the appearance of the TD-DFT $S_0 \rightarrow S_2$ band at 412 nm, with an oscillator strength 105 times greater than that of the $S_0 \rightarrow S_1$ band.

The heli-viologens 1^{2+} and 2^{2+} and their heli-bipyridine precursors **4** and **11** all fluoresce with modest but larger quantum yields and lifetimes than those reported for methyl viologen ($\Phi_F = 0.03 \pm 0.01$; $\tau_F = 1 \pm 0.04$ ns).²⁵ The fluorescence quantum yields for both heli-viologens were 2.1 times smaller than for their heli-bipyridine precursor (Table 4). On the other hand, the measured lifetime for 2^{2+} , 10.2 ± 0.6 ns, is substantially larger than the lifetime measured for 1^{2+} (5.8 ± 0.6 ns). The fluorescence lifetime measurement for 2^{2+} , however, is complicated by the fact that the sample was contaminated with approximately 3% of its photochemical closure product, 15^{2+} . Pure 15^{2+} has an emission maximum at 488 nm and a fluorescence quantum yield of 0.47 ± 0.2 . Consequently, its contribution to the fluorescence intensity is substantial and the two fluorescence contributors were first deconvoluted (see Supporting Information) prior to calculation of Φ_F for 2^{2+} . We believe that this procedure leads to an accurate determination of Φ_F for 2^{2+} for several reasons: (1) the fluorescence lifetime, τ_F , of 15^{2+} is 7.0 ns, which is smaller than the deconvoluted τ_F of 10.2 ± 0.6 for 2^{2+} precluding any quenching of $1(2^{2+})^*$ by the contaminant, and (2) this deconvoluted lifetime and all the lifetimes reported in Table 4, when coupled with the fluorescence quantum yields, give natural radiative rate constants, k_q^0 , of the magnitude anticipated for a $\pi\pi^*$ transition.⁵³ The fluorescence of 1^{2+} was quenched with electron-rich aromatic compounds such as benzene [$E_{S_1} = 110$ kcal/mol, $k_q = (1.41 \pm 0.23) \times 10^8$ M⁻¹ s⁻¹], toluene [$E_{S_1} = 106$ kcal/mol, $k_q = (8.68 \pm 0.16) \times 10^9$ M⁻¹ s⁻¹], anisole [$E_{S_1} = 101$ kcal/mol, $k_q = (1.68 \pm 0.14) \times 10^{10}$ M⁻¹ s⁻¹], anthracene [$E_{S_1} = 76$ kcal/mol, $k_q = (2.5 \pm 1.7) \times 10^{10}$ M⁻¹ s⁻¹], and naphthalene [$E_{S_1} = 92$ kcal/mol, $k_q = (2.2 \pm 0.55) \times 10^{10}$ M⁻¹ s⁻¹].⁵⁵ The singlet energies of all these quenchers are larger than the singlet energy of 1^{2+} (Table 4) and consequently are electron/charge transfer events. In addition, the reduction potential of 1^{2+} (-0.22 V vs SCE)⁵⁶ coupled to its excited state energy (Table 4) suggests that the singlet

excited state of 1^{2+} is a potent oxidant capable of oxidizing any organic substrate with an ionization potential of less than 2.35 eV.

The heli-viologens 1^{2+} and 2^{2+} , their bipyridine precursors **4** and **11**, and bis-*N*-oxide **14** all undergo intersystem crossing to triplet excited states that are phosphorescent in ethanol glass at -196 °C (see Supporting Information). The emissions of the heli-viologens are bathochromic of the emissions of their bipyridine precursors. In addition, the phosphorescence lifetimes of 1^{2+} and 2^{2+} are 28 and 88 ms, respectively, significantly shorter than observed for **4** (1.7 s) and **11** (1.2 s). The singlet–triplet energy gaps (ΔE_{S-T}) for 1^{2+} and 2^{2+} , 5.3 and 2.5 kcal/mol, respectively, are significantly smaller than observed for **4** and **11**, 13.9 ± 0.2 and 14 ± 2 kcal/mol, respectively (Table 4). All of these ΔE_{S-T} are significantly smaller than the 20–30 kcal/mol observed for many planar aromatic hydrocarbons.⁵⁵ On the other hand, the ΔE_{S-T} for the helical bipyridines are comparable to those reported for [5]helicene ($E_{S_1} = 71.2$ kcal/mol; $\Delta E_{S-T} = 14.9$ kcal/mol) and for [6]helicene ($E_{S_1} = 69.6$ kcal/mol; $\Delta E_{S-T} = 15.1$ kcal/mol).⁵⁷ The absorption maxima [436 nm ($\epsilon = 0.32 \times 10^4$ M⁻¹ cm⁻¹)], 415 nm ($\epsilon = 0.30 \times 10^4$ M⁻¹ cm⁻¹)], fluorescence wavelength ($\lambda_F = 491$ nm), phosphorescence wavelength ($\lambda_{Phos} = 525$ nm), singlet energy ($E_{S_1} = 62.5 \pm 0.1$ kcal/mol), and triplet energy ($E_{T_1} = 55 \pm 2$ kcal/mol) of *N*-methyl-5,10-diaza[5]helicene tetrafluoroborate were distinctly different from the values for 1^{2+} (Table 4) and midway between the values of 1^{2+} and its bipyridine precursor **4**. This eliminates the possibility that the observed emissions for 1^{2+} were from a small amount of monoalkylated diazahelicene contaminant.

The ΔE_{S-T} of 23 kcal/mol for the bis-*N*-oxide **14** ($E_{S_1} = 66$ kcal/mol; $E_{T_1} = 43 \pm 2$ kcal/mol) is abnormally large in comparison to the ΔE_{S-T} for 1^{2+} and 2^{2+} , and on the basis of expectations from the energy gap law,⁵³ its quantum yield for fluorescence ($\Phi_F = 0.016$) is abnormally small. It is tempting to suggest that the bis-*N*-oxide has a spectroscopically unobserved (phantom) triplet [$T_2(\pi\pi^*)$] nearly isoenergetic with S_1 (Figure 12). The $S_0 \rightarrow S_1$ transition in **14** has a significant amount of $n\pi^*$ character (Figure 12), so intersystem crossing to $T_2(\pi\pi^*)$ would be allowed by El-Sayed's rules.^{58–60} Consequently, competing fluorescence would be more effectively quenched than in the viologens 1^{2+} and 2^{2+} that

must intersystem cross by an El-Sayed disallowed $S_1(\pi\pi^*) \rightarrow T_1(\pi\pi^*)$ process.

CONCLUSIONS

The first example of isomeric helical viologens has been reported, and their structures, racemization rates, photochemistry, and photophysical properties have been presented and compared. These new molecules have a variety of potential applications, including their incorporation into molecular machines and their use as chiral hosts^{11,61} for electron-rich guests.⁶²

EXPERIMENTAL SECTION

General. Fluorescence spectra were recorded in acetonitrile by irradiation into the $S_0 \rightarrow S_1$ absorption band using excitation and emission slit widths of 5 nm. Fluorescence quantum yields were determined using diphenylanthracene ($\Phi = 0.90$) and anthracene ($\Phi = 0.27$) as standards.^{63,64} Phosphorescence spectra and lifetimes were collected at -196°C in ethanol glass. Fluorescence lifetimes were collected using a pulsed 340 nm LED lamp and a 400 nm cutoff filter. The fluorescence lifetime instrument response function (IRF) was collected with a dilute colloidal silica solution. High-resolution mass spectra were collected using TOF-TOF-MALDI. The X-ray data were measured at 150 K with a CCD detector system equipped with a graphite monochromator and a Mo $K\alpha$ fine-focus sealed tube operated at 1.5 kW power (50 kV, 30 mA). The structure of 2^{2+} was solved by direct methods using the SHELXTL (V. 2014.11-0) software package. All of the non-hydrogen atoms were refined anisotropically, and the hydrogen atoms were placed in calculated positions and refined isotropically by adapting a riding model with fixed thermal parameters. The final refinement parameters are $R_1 = 0.0745$ and $wR_2 = 0.2156$ for data with $F > 4\sigma(F)$ giving the data to parameter ratio of 24. The refinement for all data are $R_1 = 0.0989$ and $wR_2 = 0.2443$. All calculations were done using either the Gaussian 03 or Gaussian 09 program packages (see Supporting Information). Geometry optimizations were done using DFT in conjunction with the B3LYP functional and the 6-311+G(2d,p) basis set. All structures reported are stationary points, as verified by frequency calculations that revealed either one or zero negative frequencies. When solvent was included, the polarizable continuum model and polarizable conductor calculations as implemented in the Gaussian computation package were used.

(E)-1,2-Di(quinolin-3-yl)ethene (3).^{37,38} A mixture of 0.4 mL of triethoxy(vinyl)silane and 15 mL of 0.5 M aqueous sodium hydroxide was added to a 100 mL pressure vessel followed by 0.416 mL (3.0 mmol) of 3-bromoquinoline and 2.0 mg (9 μmol) of palladium(II) acetate. The vessel was then sealed and warmed at 140°C for 3–5 h. When the reaction cooled to room temperature the green precipitate was filtered and washed with ethyl acetate/chloroform 10:1. The yellow solid was then dried in vacuum. Yield: 0.38 g (2.7 mmol, 91%). $^1\text{H NMR}$ (400 MHz, CDCl_3): δ 9.20 (d, 2H, $J = 2.1$ Hz), 8.26 (d, 2H, $J = 2.1$ Hz), 8.11 (d, 2H, $J = 8.4$ Hz), 7.86 (d, 2H, $J = 7.9$ Hz), 7.72 (ddd, 2H, $J = 8.4, 7.0, 1.5$ Hz), 7.58 (ddd, 2H, $J = 8.1$ Hz, 6.8 Hz, 0.9 Hz), 7.48 (s, 2H) ppm.

5,10-Diaza[5]helicene (4)³⁶ and Benzo[b]-1,8-diaza[4]-helicene (5). (E)-1,2-Di(quinolin-3-yl)ethane (3) (0.282 g, 1.0 mmol) was dissolved in ethyl acetate (150 mL) in a Pyrex vessel open to air. The solution was irradiated with UV light for 24 h. The irradiation was then stopped and the solvent removed under reduced pressure. The residue was purified by column chromatography (eluent was ethyl acetate:hexane = 5:1). Yield: 0.186 g (0.66 mmol, 66%). $^1\text{H NMR}$ (400 MHz, CDCl_3): δ 9.44 (s, 2H), 8.61 (dd, 2H, $J = 8.3, 1.0$ Hz), 8.28 (dd, 2H, $J = 8.2, 1.2$ Hz), 8.11 (s, 2H), 7.74 (ddd, 2H, $J = 8.4, 7.1, 1.3$ Hz), 7.41 (ddd, 2H, $J = 8.5, 7.2, 1.3$ Hz). Benzo[b]-1,8-diaza[4]helicene (5) was found as a byproduct in the above reaction. It was also isolated by column chromatography and recrystallized from acetone. Yield: 0.028 g (0.10 mmol, 10%). $^1\text{H NMR}$ (400 MHz, CDCl_3): δ 11.45 (d, 1H, $J = 8.5$ Hz), 9.45 (s, 1H), 8.87 (s, 1H), 8.58 (d, 1H, $J = 8.6$ Hz), 8.35 (d, 1H, $J = 8.2$ Hz), 8.11 (m, 2H), 7.85–8.01

(m, 4H), 7.70 (dd, 1H, $J = 7.4, 7.3$ Hz) ppm. $^{13}\text{C NMR}$ (400 MHz, CDCl_3): δ 152.5, 148.4, 148.3, 147.7, 147.6, 136.3, 130.6, 130.5, 130.4, 130.3, 129.0, 128.6, 128.3, 128.0, 127.8, 127.7, 127.4, 126.7, 126.1, 126.0 ppm. Anal. Calcd for $\text{C}_{20}\text{H}_{12}\text{N}_2$: 85.69% C, 4.31% H, 9.99% N. Found: 85.52% C, 4.47% H, 9.83% N.

***N,N'*-Dimethyl-5,10-diaza[5]helicene Bis-tetrafluoroborate (1²⁺).** 5,10-Diaza[5]helicene (4) (40 mg, 0.14 mmol) was dissolved in 30 mL of dichloromethane saturated with dry N_2 gas. Trimethyloxonium tetrafluoroborate (55 mg, 0.37 mmol) was then added. The mixture was stirred in a nitrogen atmosphere for 24 h. The solvent was then removed under reduced pressure. The yellow crude product was triturated in warm 95% ethanol. It was then dried in vacuum for 12 h. Yield: 50 mg (0.10 mmol, 73%). $^1\text{H NMR}$ (400 MHz, CD_3CN): δ 10.07 (d, 2H, $J = 2.2$ Hz), 8.75 (d, 2H, $J = 8.3$ Hz), 8.71 (d, 2H, $J = 1.7$ Hz), 8.61 (d, 2H, $J = 8.8$ Hz), 8.27 (ddd, 2H, $J = 8.6, 7.1, 1.2$ Hz), 7.89 (ddd, 2H, $J = 8.3, 7.1, 0.9$ Hz), 4.86 (s, 6H) ppm. $^{13}\text{C NMR}$ (600 MHz, $\text{DMSO}-d_6$): δ 154.9, 135.3, 133.6, 131.5, 130.9, 129.3, 128.6, 127.9, 125.6, 119.7, and 46.1 ppm. Anal. Calcd for $\text{C}_{22}\text{H}_{18}\text{N}_2\text{B}_2\text{F}_8$: 54.59% C, 3.75% H, 5.79% N. Found: 54.35% C, 3.74% H, 5.82% N. It decomposes with a gradual color change starting at 200°C to finally form a black solid without ever clearly melting within the temperature range of our melting point apparatus.

***N*-Methyl-5,10-diaza[5]helicene Tetrafluoroborate (13⁺).** *N,N'*-Dimethyl-5,10-diaza[5]helicene bis-tetrafluoroborate (1²⁺) (30 mg, 0.07 mmol) was added to 10 mL of deionized water and refluxed for 1 h. After the solution was cooled to room temperature, the solid was removed by filtration. The solvent was then removed under vacuum. The residue was recrystallized from ethanol and dried in vacuum. A yellow solid (5 mg) was collected. Yield: 22% contaminated with approximately 10% of 12⁺. $^1\text{H NMR}$ (400 MHz, CD_3CN): δ 9.90 (s, 1H), 9.68 (s, 1H), 8.95 (d, 1H, $J = 8.5$ Hz), 8.55 (d, 1H, $J = 8.3$ Hz), 8.52 (d, 1H, $J = 8.7$ Hz), 8.51 (d, 1H, $J = 8.4$ Hz), 8.49 (d, 1H, $J = 8.3$ Hz), 8.37 (dd, 1H, $J = 8.3, 1.2$ Hz), 8.18 (ddd, 1H, $J = 8.6, 7.2, 1.3$ Hz), 7.93 (ddd, 1H, $J = 8.3, 7.0, 1.3$ Hz), 7.84 (ddd, 1H, $J = 8.3, 7.1, 1.1$ Hz), 7.59 (ddd, 1H, $J = 8.4, 7.0, 1.4$ Hz), 4.77 (s, 3H) ppm. $^{13}\text{C NMR}$ (400 MHz, CD_3CN): δ 154.6, 153.5, 147.4, 136.2, 134.8, 134.2, 131.7, 131.6, 131.2, 130.9, 130.0, 129.9, 129.5, 129.2, 127.8, 127.6, 127.4, 127.2, 124.3, 120.0, 46.9. HRMS (TOF/TOF MALDI) m/z : $[\text{M}]^+$ calcd for $\text{C}_{21}\text{H}_{15}\text{N}_2$ 295.1235, found 295.1210.

2-Acetonaphthone Oxime.⁶⁵ 2-Acetonaphthone (20 g, 0.118 mol), hydroxylamine hydrochloride (8.3 g, 0.12 mol), and sodium acetate (9.8 g, 0.12 mol) were dissolved in a mixture of 30 mL of absolute ethanol and 9 mL of water. The mixture was then heated at 50°C for 20 min. The white precipitate was collected by filtration and washed with deionized water (20 mL \times 3). It was then dried in vacuum. Yield: 20.3 g (0.111 mol, 94%). $^1\text{H NMR}$ (400 MHz, CDCl_3): δ 7.95 (s, 1H), 7.77–7.87 (m, 4H), 7.44–7.50 (m, 2H), 2.33 (s, 3H) ppm.

2-Acetamidonaphthalene.⁶⁵ 2-Acetonaphthone oxime (18.5 g, 0.1 mol) was added slowly with mechanical stirring to 50 mL of polyphosphoric acid in a 200 mL beaker. The mixture was heated to 70°C and kept at this temperature for 2 h. The mixture was then poured into 300 mL of deionized water. A white precipitate was obtained by filtration. The white solid was washed with deionized water and dried in vacuum. Yield: 14.0 g (0.076 mol, yield 76%). $^1\text{H NMR}$ (400 MHz, CDCl_3): δ 8.17 (s, 1H), 7.77 (m, 2H), 7.35–7.50 (m, 4H), 2.22 (s, 3H) ppm.

2-Naphthylamine (7).⁶⁵ 2-Acetamidonaphthalene (14 g, 0.076 mol) was dissolved in a mixture of 20 mL of absolute ethanol and 8 mL of concentrated hydrochloric acid. The mixture was refluxed for 1 h and then cooled to room temperature. The solution was adjusted to $\text{pH} > 7$ by a 6 M NaOH aqueous solution. The brown precipitate was collected by filtration, washed with water, and then dried in vacuum for 6 h. White crystals were obtained by sublimation. Yield: 10.0 g (0.070 mmol, 92%). $^1\text{H NMR}$ (400 MHz, CDCl_3): δ 7.69 (d, 1H, $J = 8.2$ Hz), 7.66 (d, 1H, $J = 8.7$ Hz), 7.59 (d, 1H, $J = 8.3$ Hz), 7.39 (m, 1H), 7.24 (m, 1H), 6.99 (d, 1H, $J = 7.0$ Hz), 6.95 (dd, 1H, $J = 8.5, 2.5$ Hz), 3.75 (br s, 2H) ppm.

(3-Methyl)benzo[*f*]quinoline (6).⁴⁰ A stirred solution of $\text{RuCl}_3 \cdot x\text{H}_2\text{O}$ (52 mg, 0.20 mmol), $\text{MgBr}_2 \cdot \text{OEt}_2$ (52 mg, 0.20 mmol), PBU_3

(100 μ L, 0.40 mmol), 2-naphthylamine (**7**) (564 mg, 4.0 mmol), and 2-methyl-1,3-propanediol (426 μ L, 4.8 mmol) in anhydrous mesitylene (2 mL) was refluxed under an argon atmosphere for 16 h. The reaction mixture was then cooled to room temperature and purified by column chromatography (toluene:ethyl acetate = 1:1) on silica gel pretreated with 0.1% of Et₃N in toluene. Yield: 289 mg (1.50 mmol, 38%). ¹H NMR (400 MHz, CDCl₃): δ 8.80 (d, 1H, *J* = 1.8 Hz), 8.70 (s, 1H), 8.59 (d, 1H, *J* = 7.9 Hz), 7.86–7.98 (m, 3H), 7.58–7.70 (m, 2H), 2.60 (s, 3H) ppm. ¹³C NMR (400 MHz, CDCl₃): δ 151.4, 146.5, 132.1, 131.0, 130.4, 130.0, 129.7, 128.9, 128.3, 127.4, 127.0, 125.3, 122.8, 19.2 ppm.

(3-Bromomethyl)benzo[f]quinoline hydrobromide. (3-Methyl)benzo[f]quinoline (**6**) (289 mg, 1.50 mmol), NBS (294 mg, 1.65 mmol), and AIBN (25 mg, 0.15 mmol) were added to 40 mL of CCl₄. The solution was then irradiated with a 100 W tungsten lamp for 4 h. The floating solid was removed by filtration. The filtrate was then kept in a refrigerator for 1 h and filtered again to remove more of the byproduct succinimide. All attempts to isolate the product, 3-bromomethylbenzo[f]quinoline, failed due to polymerization unless it was first converted to the hydrobromide salt, in situ, by bubbling HBr gas through the solution. The yellow precipitate was collected and the filtrate treated with additional HBr gas to produce more yellow precipitate. The precipitate fractions were combined and washed with DCM. After drying in vacuum for 12 h, it was used directly for the next step without characterization.

3-((Triphenylphosphonio)methyl)benzo[f]quinolin-4-ium Dibromide.⁶⁶ The (3-bromomethyl)benzo[f]quinoline hydrobromide collected from the previous step and triphenylphosphine (393 mg, 1.5 mmol) were added to 20 mL of acetonitrile and refluxed overnight. The brown solid was filtered and washed with 5 mL of acetonitrile and 5 mL of ethyl acetate. It was then air-dried and used directly for the next step without characterization.

(E)-1-(Benzo[f]quinolin-3-yl)-2-(3-pyridyl)ethene (8**).**⁶⁶ Sodium (92 mg, 4 mmol) was added slowly to 10 mL of methanol at 0 °C. After all the sodium reacted, the 3-((triphenylphosphonio)methyl)benzo[f]quinolin-4-ium dibromide collected from the previous step was added in portions to the reaction mixture. The mixture was stirred at 0 °C for 1 h before addition of 3-pyridinecarboxaldehyde (162 mg, 1.5 mmol). The reaction mixture was then warmed to reflux and kept under reflux overnight. Then 30 mL of aqueous 10% HCl solution was added slowly to the reaction. The mixture was extracted with ethyl acetate to remove most of the triphenylphosphine oxide (20 mL \times 3). The aqueous layer was then basified by 2 M NaOH and then extracted again with ethyl acetate (30 mL \times 3). The organic layers were combined and dried over MgSO₄. The solvent was then removed under reduced pressure. The residue was purified by column chromatography (eluent was ethyl acetate:hexane = 3:1). Yield of three steps: 242 mg (0.86 mmol, 57%). ¹H NMR (400 MHz, CDCl₃): δ 8.79 (m, 2H), 8.57 (d, 1H, *J* = 1.9 Hz), 8.49 (dd, 1H, *J* = 4.9, 1.5 Hz), 8.33 (m, 1H), 7.90–8.01 (m, 3H), 7.64 (m, 2H), 7.58 (d, 1H, *J* = 8.0 Hz), 7.15 (dd, 1H, *J* = 7.7, 4.8 Hz), 6.97 (d, 1H, *J* = 12.2 Hz), 6.85 (d, 1H, *J* = 12.1 Hz) ppm. ¹³C NMR (400 MHz, CDCl₃): δ 150.2, 150.1, 149.4, 148.8, 135.6, 132.6, 132.5, 131.9, 131.1, 130.2, 129.9, 129.5, 129.3, 129.0, 128.8, 127.9, 127.5, 127.3, 123.3, 122.4 ppm.

3,8-Diaza[5]helicene (11**), 1,8-Diaza[5]helicene (**9**), and Benzo[a]pyrido[4,3-*h*]acridine (**10**).** (E)-1-(benzo[f]quinolin-3-yl)-2-(3-pyridyl)ethene (**8**) (242 mg, 0.86 mmol) was dissolved in 300 mL of ethyl acetate and irradiated with UV light for 24 h. The solvent was then removed under reduced pressure. The residue was then purified by column chromatography (eluent was ethyl acetate:hexane = 3:1 gradually increased to 5:1). Three products were isolated, i.e., 3,8-diaza[5]helicene (**11**), 1,8-diaza[5]helicene (**9**), and benzo[a]pyrido[4,3-*h*]acridine (**10**). Data for 3,8-diaza[5]helicene (**11**): Yield 91 mg (0.33 mmol, 38%). ¹H NMR (400 MHz, CDCl₃): δ 9.42 (d, 1H, *J* = 0.8 Hz), 9.40 (s, 1H), 8.51 (m, 2H), 8.42 (d, 1H, *J* = 6.0 Hz), 8.09–8.19 (m, 4H), 8.03 (dd, 1H, *J* = 8.0, 1.3 Hz), 7.64 (ddd, 1H, *J* = 8.1, 7.6, 1.2 Hz), 7.41 (ddd, 1H, *J* = 8.5, 8.1, 1.4 Hz) ppm. ¹³C NMR (400 MHz, CDCl₃): δ 152.4, 151.7, 146.4, 143.4, 133.2, 132.9, 130.5, 129.4, 129.2, 128.8, 128.7, 128.2, 127.7, 127.6, 127.5, 126.9, 126.1, 125.1, 120.9, 120.8 ppm. Data for 1,8-diaza[5]helicene (**9**):

Yield 84 mg (0.30 mmol, 35%). ¹H NMR (400 MHz, CDCl₃): δ 9.41 (s, 1H), 8.80 (dd, 1H, *J* = 4.2, 1.8 Hz), 8.34 (m, 2H), 8.08–8.17 (m, 3H), 8.00 (d, 1H, *J* = 8.5 Hz), 7.97 (d, 1H, *J* = 8.0 Hz), 7.57–7.64 (m, 2H), 7.35 (ddd, 1H, *J* = 8.6, 7.2, 1.3 Hz) ppm. ¹³C NMR (400 MHz, CDCl₃): δ 151.1, 147.4, 146.8, 145.4, 136.0, 132.8, 131.7, 130.9, 130.7, 130.4, 128.8, 128.0, 127.4, 127.3, 127.2, 127.0, 125.8, 123.5, 123.4, 121.3 ppm. HRMS (TOF/TOF MALDI) *m/z*: [M]⁺ calcd for C₂₀H₁₃N₂ 281.1079, found 281.1095. Data for benzo[4,3-*h*]pyrido[*a*]acridine (**10**): Yield 43 mg (0.15 mmol, 18%). ¹H NMR (400 MHz, CDCl₃): δ 9.46 (s, 1H), 9.32 (s, 1H), 9.26 (d, 1H, *J* = 5.4 Hz), 8.94 (d, 1H, *J* = 5.4 Hz), 8.85 (d, 1H, *J* = 8.0 Hz), 8.23 (d, 1H, *J* = 9.3 Hz), 8.09 (d, 1H, *J* = 9.2 Hz), 8.04 (d, 1H, *J* = 8.9 Hz), 8.00 (d, 1H, *J* = 7.9 Hz), 7.91 (d, 1H, *J* = 8.9 Hz), 7.80 (dd, 1H, *J* = 7.6, 7.2 Hz), 7.74 (dd, 1H, *J* = 7.3, 7.2 Hz) ppm. The limited solubility of **10** prevents acquisition of a ¹³C NMR spectrum in a reasonable amount of time. HRMS (TOF/TOF MALDI) *m/z*: [M]⁺ calcd for C₂₀H₁₃N₂ 281.1079, found 281.1082.

***N,N'*-Dimethyl-3,8-diaza[5]helicene Bis-tetrafluoroborate (**2²⁺**).** 3,8-Diaza[5]helicene (**11**) (91 mg, 0.33 mmol) was dissolved in 20 mL of dry DCM. Trimethyloxonium tetrafluoroborate (147 mg, 1 mmol) was then added to this solution. The mixture was stirred under a nitrogen atmosphere for 24 h. Ethanol (2 mL) was then added to quench the excess trimethyloxonium tetrafluoroborate. The solid was then filtered and triturated with absolute ethanol. The red solid was then filtered and dried in vacuum for 12 h. Yield: 112 mg (0.23 mmol, 70%). ¹H NMR (400 MHz, CD₃CN): δ 9.88 (s, 1H), 9.75 (s, 1H), 8.97 (d, 1H, *J* = 6.8 Hz), 8.72 (d, 1H, *J* = 9.2 Hz), 8.67 (d, 1H, *J* = 8.7 Hz), 8.64 (d, 1H, *J* = 8.8 Hz), 8.53 (d, 1H, *J* = 8.7 Hz), 8.43 (d, 1H, *J* = 9.3 Hz), 8.39 (d, 1H, *J* = 6.9 Hz), 8.36 (d, 1H, *J* = 8.0 Hz), 7.98 (ddd, 1H, *J* = 7.6, 7.8, 0.9 Hz), 7.66 (dd, 1H, *J* = 7.9, 7.4, 1.0 Hz), 4.81 (s, 3H), 4.53 (s, 3H) ppm. ¹³C NMR (400 MHz, CD₃CN): δ 151.8, 151.0, 138.7, 138.8, 137.6, 136.7, 134.4, 133.9, 132.5, 132.1, 131.0, 130.9, 130.1, 130.0, 129.7, 129.5, 128.9, 127.7, 126.3, 116.5, 49.8, 48.2 ppm.

(2,7-Dimethyl-2,7-diaza)benzo[ghi]perylene Bis-tetrafluoroborate (15²⁺**).** *N,N'*-Dimethyl-3,8-diaza[5]helicene bis-tetrafluoroborate (**2²⁺**) (20 mg, 0.041 mmol) was dissolved in 20 mL of acetonitrile. The solution was irradiated with visible light (ambient light) for 48 h. The solution was concentrated to about 5 mL followed by addition of 5 mL of diethyl ether. The yellow precipitate was filtered and dried in vacuum. Yield: 18 mg (0.037 mmol, 90%). ¹H NMR (400 MHz, CD₃CN): δ 10.36 (s, 1H), 10.27 (s, 1H), 9.84 (s, 1H), 9.56 (d, 1H, *J* = 7.8 Hz), 9.11 (d, 1H, *J* = 9.5 Hz), 8.98 (d, 1H, *J* = 7.8 Hz), 8.90 (d, 1H, *J* = 9.1 Hz), 8.81 (d, 1H, *J* = 9.5 Hz), 8.76 (d, 1H, *J* = 9.0 Hz), 8.64 (dd, 1H, *J* = 8.0, 7.9 Hz), 5.06 (s, 3H), 4.89 (s, 3H) ppm. The limited solubility of **15²⁺** prevents acquisition of a ¹³C NMR spectrum in a reasonable amount of time. HRMS (MALDI/TOF-TOF) *m/z*: calcd for C₂₂H₁₆N₂²⁺ 308.13135, found 308.1325.

5,10-Diaza[5]helicene *N,N'*-Bisoxide (14**).**⁶⁷ Under vigorous magnetic stirring, 3-chloroperbenzoic acid (*m*-CPBA) (345 mg, 2 mmol) in CH₂Cl₂ (5 mL) was added dropwise into a solution of 5,10-diaza[5]helicene (280 mg, 1 mmol) in CH₂Cl₂ (5 mL) at 0 °C. After the addition, the reaction was warmed to room temperature and stirred overnight. An aqueous solution of saturated NaHCO₃ was added to the mixture to neutralize the unreacted *m*-CPBA. The resulting mixture was extracted with CH₂Cl₂ (3 \times 10 mL). The organic phase were combined and washed with saturated NaCl solution (3 \times 5 mL). The organic layer was dried over anhydrous MgSO₄, filtered, and evaporated under reduced pressure to give crude product. The crude product was purified by trituration with chloroform followed by recrystallization from methanol and dried in vacuum. Yield: 169 mg (0.55 mmol, 55%). ¹H NMR (400 MHz, CD₃CN): δ 8.93 (s, 2H), 8.79 (d, 2H, *J* = 8.6 Hz), 8.57 (d, 2H, *J* = 8.3 Hz), 7.91 (s, 2H), 7.85 (m, 2H), 7.55 (m, 2H) ppm. ¹³C NMR (400 MHz, CD₃CN): δ 141.8, 134.9, 131.8, 129.9, 129.4, 128.8, 127.9, 127.6, 123.7, 120.8 ppm.

■ ASSOCIATED CONTENT

■ Supporting Information

The Supporting Information is available free of charge on the ACS Publications website at DOI: 10.1021/acs.joc.6b00835.

Computational details; X-ray crystallographic analysis; fluorescence deconvolution of 15^{2+} ; fluorescence, absorption, and phosphorescence spectra of N-methyl-5,10-diaza[5]helicene tetrafluoroborate; and ^{13}C and ^1H NMR spectra (PDF)

Crystallographic data in CIF format for 1^{2+} and 2^{2+} (CIF)

■ AUTHOR INFORMATION

Corresponding Author

*E-mail: clennane@uwyo.edu

Notes

The authors declare no competing financial interest.

■ ACKNOWLEDGMENTS

We thank the National Science Foundation (CHE-1147542) for their generous support of this research.

■ REFERENCES

- Weidel, H.; Russo, M. *Monatsh. Chem.* **1882**, *3*, 850.
- Monk, P. M. S. *The Viologens. Physicochemical Properties, Synthesis and Applications of the Salts of 4,4'-Bipyridine*; John Wiley & Sons: Chichester, England, 1998.
- Summers, L. A. *The Bipyridinium Herbicides*; Academic Press: New York, 1980.
- Summers, L. A. In *Advances in Heterocyclic Chemistry*; Katritzky, A. R., Ed.; Academic Press: Orlando, FL, 1984; Vol. 35, p 281.
- Boßmann, S.; Seiler, M.; Dürr, H. J. *Phys. Org. Chem.* **1992**, *5*, 63.
- Contreras Carballada, P.; Mourtzis, N.; Felici, M.; Bonnet, S.; Nolte, R. J. M.; Williams, R. M.; De Cola, L.; Feiters, M. C. *Eur. J. Org. Chem.* **2012**, *2012*, 6729.
- Xu, C.; Mochizuki, D.; Maitani, M. M.; Wada, Y. *Eur. J. Inorg. Chem.* **2014**, *2014*, 1470.
- Lorente, A.; Fernández-Saiz, M.; Herraiz, F.; Lehn, J.-M.; Vigneron, J.-P. *Tetrahedron Lett.* **1999**, *40*, 5901.
- Bachrach, S. M. *J. Phys. Chem. A* **2013**, *117*, 8484.
- Bachrach, S. M.; Nickle, Z. O. M. *J. Phys. Chem. A* **2015**, *119*, 10613.
- Barnes, J. C.; Juríček, M.; Strutt, N. L.; Frasconi, M.; Sampath, S.; Giesener, M. A.; McGrier, P. L.; Bruns, C. J.; Stern, C. L.; Sarjeant, A. A.; Stoddart, J. F. *J. Am. Chem. Soc.* **2013**, *135*, 183.
- Fahrenbach, A. C.; Barnes, J. C.; Lanfranchi, D. A.; Li, H.; Coskun, A.; Gassensmith, J. J.; Liu, Z.; Benítez, D.; Trabolsi, A.; Goddard, W. A.; Elhabiri, M.; Stoddart, J. F. *J. Am. Chem. Soc.* **2012**, *134*, 3061.
- Jalilov, A. S.; Patwardhan, S.; Singh, A.; Simeon, T.; Sarjeant, A. A.; Schatz, G. C.; Lewis, F. D. *J. Phys. Chem. B* **2014**, *118*, 125.
- Clennan, E. L. *Coord. Chem. Rev.* **2004**, *248*, 477.
- Deng, J.; Zhou, C.; Song, N. *Macromolecules* **2009**, *42*, 6865.
- Coskun, A.; Spruell, J. M.; Barin, G.; Dichtel, W. R.; Flood, A. H.; Botros, Y. Y.; Stoddart, J. F. *Chem. Soc. Rev.* **2012**, *41*, 4827.
- Kaur, K.; Mittal, S. K.; Kumar, S. K.; Kumar, A.; Kumar, S. *Anal. Methods* **2013**, *5*, 5565.
- Li, H.-Y.; Wei, Y.-L.; Dong, X.-Y.; Zang, S.-Q.; Mak, T. C. W. *Chem. Mater.* **2015**, *27*, 1327.
- Tong, J.; Guo, X.; Jia, L.; Tian, X. *Mater. Lett.* **2015**, *158*, 255.
- Sun, J.; Wu, Y.; Wang, Y.; Liu, Z.; Cheng, C.; Hartlieb, K. J.; Wasielewski, M. R.; Stoddart, J. F. *J. Am. Chem. Soc.* **2015**, *137*, 13484.
- Boydston, A. J.; Pecinovsky, C. S.; Chao, S. T.; Bielawski, C. W. *J. Am. Chem. Soc.* **2007**, *129*, 14550.
- Boydston, A. J.; Vu, P. D.; Dykhno, O. L.; Chang, V.; Wyatt, A. R.; Stockett, A. S.; Ritschdorff, E. T.; Shear, J. B.; Bielawski, C. W. *J. Am. Chem. Soc.* **2008**, *130*, 3143.
- Henrich, J. D.; Suchyta, S.; Kohler, B. *J. Phys. Chem. B* **2015**, *119*, 2737.
- Hohenstein, E. G. *J. Am. Chem. Soc.* **2016**, *138*, 1868.
- Peon, J.; Tan, X.; Hoerner, J. D.; Xia, C.; Luk, Y. F.; Kohler, B. *J. Phys. Chem. A* **2001**, *105*, 5768.
- Lin, F.; Zhao, X. *Tetrahedron* **2015**, *71*, 1124.
- A preliminary accounting of some of the work reported here: Zhang, X.; Clennan, E. L.; Arulsamy, N. *Org. Lett.* **2014**, *16*, 4610.
- Takahama, H.; Tanaka, M.; Hasegawa, Y.; Tsukahara, K. *J. Biol. Inorg. Chem.* **2003**, *8*, 499.
- Tsukahara, K.; Goda, M. *Chem. Lett.* **1998**, 929.
- Tsukahara, K.; Kaneko, J.; Miyaji, T.; Abe, K. *Tetrahedron Lett.* **1996**, *37*, 3149.
- Tsukahara, K.; Ueda, R.; Goda, M. *Bull. Chem. Soc. Jpn.* **2001**, *74*, 1303.
- Adriaenssens, L.; Severa, L.; Šalová, T.; Císařová, I.; Pohl, R.; Šaman, D.; Rocha, S. V.; Finney, N. S.; Pospíšil, L.; Slaviček, P.; Teplý, F. *Chem. - Eur. J.* **2009**, *15*, 1072.
- Nath, N. K.; Severa, L.; Kunetskiy, R. A.; Císařová, I.; Fulem, M.; Růžička, K.; Koval, D.; Kašička, V.; Teplý, F.; Naumov, P. *Chem. - Eur. J.* **2015**, *21*, 13508.
- Reyes-Gutierrez, P. E.; Jirasek, M.; Severa, L.; Novotna, P.; Koval, D.; Sazelova, P.; Vavra, J.; Meyer, A.; Cisarova, I.; Saman, D.; Pohl, R.; Stepanek, P.; Slavicek, P.; Coe, B. J.; Hajek, M.; Kasicka, V.; Urbanova, M.; Teplý, F. *Chem. Commun.* **2015**, *51*, 1583.
- Sonawane, M. R.; Vávra, J.; Šaman, D.; Císařová, I.; Teplý, F. *Synthesis* **2015**, *47*, 3479.
- Bazzini, C.; Brovelli, S.; Caronna, T.; Gambarotti, C.; Giannone, M.; Macchi, P.; Meinardi, F.; Mele, A.; Panzeri, W.; Recupero, F.; Sironi, A.; Tubino, R. *Eur. J. Org. Chem.* **2005**, *2005*, 1247.
- Gordillo, A.; de Jesus, E.; Lopez-Mardomingo, C. *Chem. Commun.* **2007**, 4056.
- Gordillo, A.; Ortuño, M. A.; López-Mardomingo, C.; Lledós, A.; Ujaque, G.; de Jesús, E. *J. Am. Chem. Soc.* **2013**, *135*, 13749.
- Meerwein, H. In *Organic Syntheses*; Baumgarten, H. E., Ed.; John Wiley & Sons: New York, 1973; Collect. Vol. V, p 1096.
- Monrad, R. N.; Madsen, R. *Org. Biomol. Chem.* **2011**, *9*, 610.
- Mallory, F. B.; Mallory, C. W. In *Organic Reactions*; Dauben, W. G., Ed.; John Wiley & Sons: New York, 1984; Vol. 30, p 1.
- Bazzini, C.; Caronna, T.; Fontana, F.; Macchi, P.; Mele, A.; Sora, I. N.; Panzeri, W.; Sironi, A. *New J. Chem.* **2008**, *32*, 1710.
- Meyer, E. A.; Castellano, R. K.; Diederich, F. *Angew. Chem., Int. Ed.* **2003**, *42*, 1210.
- Vacek Chocholoušová, J.; Vacek, J.; Andronova, A.; Míšek, J.; Songis, O.; Šámal, M.; Stará, I. G.; Meyer, M.; Bourdillon, M.; Pospíšil, L.; Starý, I. *Chem. - Eur. J.* **2014**, *20*, 877.
- Martin, R. H.; Marchant, M. *J. Tetrahedron* **1974**, *30*, 347.
- Adam, R.; Ballesteros-Garrido, R.; Vallcorba, O.; Abarca, B.; Ballesteros, R.; Leroux, F. R.; Colobert, F.; Amigó, J. M.; Rius, J. *Tetrahedron Lett.* **2013**, *54*, 4316.
- Goedicke, C.; Stegemeyer, H. *Tetrahedron Lett.* **1970**, *11*, 937.
- Joule, J. A.; Mills, K. *Heterocyclic Chemistry*, 5th ed.; Wiley-Blackwell, 2010.
- Orlandi, G.; Zerbetto, F.; Henneker, W.; Zgierski, M. Z. *Chem. Phys. Lett.* **1986**, *129*, 296.
- The contributions of the HOMO–LUMO determinant was calculated by taking 2 times the square of the coefficient for the configuration interaction expansion. This is an approximation that ignores contributions from de-excitations.
- Nakagawa, Y.; Suzuka, I.; Ito, M. *Chem. Phys. Lett.* **1993**, *208*, 453.
- Palmer, M. H.; Findlay, R. H.; Moyes, W.; Gaskell, A. J. *J. Chem. Soc., Perkin Trans. 2 (1972-1999)* **1975**, 841.
- Turro, N. J.; Ramamurthy, V.; Scaiano, J. C. *Modern Molecular Photochemistry of Organic Molecules*; University Science Books: Sausalito, CA, 2010.

- (54) Wintgens, V. In *CRC Handbook of Organic Photochemistry*; Scaiano, J. C., Ed.; CRC Press, Inc.: Boca Raton, FL, 2000; Vol. II, p 405.
- (55) Montalti, M.; Credi, A.; Prodi, L.; Gandolfi, M. T. *Handbook of Photochemistry*, 3rd ed.; CRC Press: Boca Raton, FL, 2006.
- (56) Clennan, E. L., Zhang, X.; Petek, T. Unpublished results.
- (57) Sapir, M.; Vander Donckt, E. *Chem. Phys. Lett.* **1975**, *36*, 108.
- (58) El-Sayed, M. A. *J. Chem. Phys.* **1962**, *36*, 573.
- (59) El-Sayed, M. A. *J. Chem. Phys.* **1963**, *38*, 2834.
- (60) El-Sayed, M. A. *J. Chem. Phys.* **1964**, *41*, 2462.
- (61) Sue, C.-H.; Basu, S.; Fahrenbach, A. C.; Shveyd, A. K.; Dey, S. K.; Botros, Y. Y.; Stoddart, J. F. *Chem. Sci.* **2010**, *1*, 119.
- (62) Bernardo, A. R.; Stoddart, J. F.; Kaifer, A. E. *J. Am. Chem. Soc.* **1992**, *114*, 10624.
- (63) Eaton, D. F. In *CRC Handbook of Organic Photochemistry*; Scaiano, J. C., Ed.; CRC Press, Inc.: Boca Raton, FL, 2000; Vol. I, p 231.
- (64) Hamai, S.; Hirayama, F. *J. Phys. Chem.* **1983**, *87*, 83.
- (65) Zi, G.; Zhang, Z.; Wang, Q.; Ai, L. In *Zhuanli Shenqing Gogkai Shumingshu*; 2010; Vol. CN 101740758 A 20100512.
- (66) Dolušić, E.; Larrieu, P.; Moineaux, L.; Stroobant, V.; Pilotte, L.; Colau, D.; Pochet, L.; Van den Eynde, B.; Masereel, B.; Wouters, J.; Frédérick, R. *J. Med. Chem.* **2011**, *54*, 5320.
- (67) Li, G.; Jia, C.; Sun, K. *Org. Lett.* **2013**, *15*, 5198.